ACI STRUCTURAL JOURNAL TECHNICAL PAPER

Title no. 99-S79

Effect of Matrix Ductility on Deformation Behavior of Steel-Reinforced ECC Flexural Members under Reversed Cyclic Loading Conditions

by Gregor Fischer and Victor C. Li

This paper summarizes results of a research project aimed at investigating the effect of ductile deformation behavior of engineered cementitious composites (ECC) on the response of steel reinforced flexural members to lateral load reversals. The combination of a ductile cementitious matrix and steel reinforcement is found to result in improved energy dissipation capacity, reduction of transverse steel reinforcement requirements, and damage-tolerant inelastic deformation behavior. The basic concepts and composite deformation mechanisms of steel reinforced ECC are presented, experimentally verified, and compared to conventional reinforced concrete using small-scale specimens. Results indicate advantageous synergistic effects between ECC matrix and steel reinforcement with respect to compatible deformation, structural composite integrity, and damage evolution, and they suggest integrating advanced materials design in the structural design process. Due to the scale of the specimens used in this study, experimental results presented in this paper are interpreted from a conceptual rather than strictly quantitative viewpoint.

Keywords: damage; deformation; ductility; reinforced concrete; tolerance.

INTRODUCTION

The performance of structures required to resist seismic excitations is dependent on the ability of selected structural components—in particular flexural members such as beams and columns in a moment-resisting frame—to sustain relatively large inelastic deformations without a significant loss of load-carrying capacity. The ductility of these typical reinforced concrete components is indirectly dependent on the amount and configuration of transverse steel reinforcement, which serves as confinement of the concrete core and shear-capacity enhancement and also provides resistance against buckling of longitudinal reinforcement (Paulay and Priestley 1992; Watson, Zahn, and Park 1994; Sheikh and Yeh 1990). In essence, an increased amount of transverse reinforcement at deformation-critical locations of flexural members results in increased structural ductility by enhancing resistance to undesirable failure modes and delaying flexural strength decay under inelastic deformation reversals.

On the materials scale, the fundamental source of damage observed in reinforced concrete structures is the brittleness of concrete in general but tension in particular. Structural deficiencies associated with this material property, such as bond splitting, concrete spalling, flexural strength decay due to shear failure, brittle compression failure, and buckling of longitudinal reinforcement are usually overcome by arranging transverse reinforcement to confine concrete in compression or divert internal tensile forces from concrete to the transverse reinforcement to resist shear and prevent buckling of longitudinal reinforcement. Transverse reinforcement can be considered an external means to counteract internal material deficiencies of concrete to achieve a virtually ductile deformation behavior in tension and compression, with an increasing amount of transverse reinforcement resulting in increased structural ductility. Consequently, critical locations of structures, such as plastic hinge regions and joints, can be heavily congested and difficulties may arise in arranging the required amount of transverse reinforcement and in proper placement of concrete in these congested zones.

Despite enhanced resistance to undesirable failure modes by providing transverse reinforcement, the inherently brittle deformation behavior of concrete cannot be modified and deficiencies with respect to steel/concrete interaction, interfacial bond deterioration, and composite integrity are not overcome. Damage in reinforced concrete composites under large deformation reversals results from the inability of concrete to accommodate inelastic deformations of the steel reinforcement. These incompatible strains lead to interfacial slip, bond deterioration, and ultimately to bond splitting and spalling, which negatively affects the inelastic response of the structural member. Overcoming the deformation incompatibility of concrete and steel and its resulting effects on the structural behavior are the focus of research activities presented herein. By substituting concrete with little or no ductility with a ductile engineered cementitious composite (ECC), both constituents of the reinforced composite, longitudinal steel reinforcement and ECC, are deforming compatibly in the inelastic deformation regime. Previous investigations on the tension-stiffening effect have shown that the combination of ECC and steel reinforcement results in reduced interfacial bond stresses and elimination of bond-splitting cracks and cover spalling (Fischer and Li 2002).

In the following, the relevant material properties of ECC reinforced with polyethylene fibers as well as the interaction characteristics with steel reinforcement in uniaxial tension are briefly presented and the anticipated response of reinforced ECC under flexural loading conditions is outlined. In the subsequent sections, results of the experimental verification of this response concept are described and discussed in detail.

RESEARCH SIGNIFICANCE

In this paper, the composite resistance and deformation mechanisms of reinforced ECC (R/ECC) members under

ACI Structural Journal, V. 99, No. 6, November-December 2002.
MS No. 01-290 received September 10, 2001, and reviewed under Institute publication policies. Pertinent discussion will be published in the September-October 2003 *ACI Structural Journal* if received by May 1, 2003.

Gregor Fischer *is an assistant professor in the Department of Civil and Environmental Engineering at the University of Hawaii at Manoa. He received his PhD and MSE from the University of Michigan. His research interests include the design of fiber-reinforced cement composites and their structural applications.*

Victor C. Li *is a professor in the Department of Civil and Environmental Engineering at the University of Michigan, Ann Arbor, Mich. His research interests include micro-mechanics-based design of fiber-reinforced cementitious composites and integrated materials-structural design for performance enhancement, including repair and retrofit of infrastructures.*

flexural load reversals are investigated and compared to conventional reinforced concrete (RC). This study emphasizes understanding of the composite response mechanisms and their implications on the design of R/ECC members rather than suggesting explicit design guidelines. The evaluation of composite performance focuses on flexural strength, ductility, energy dissipation, and failure modes as well as other indices, such as curvature distribution, extent of damage, and matrix/reinforcement interaction. In particular, the direct contributions of the tensile capacity of ECC to flexural strength, energy dissipation, confinement effect, and shear resistance of the reinforced member are identified and characterized.

The knowledge derived from this study provides a conceptual basis for design of R/ECC members for seismic resistant structures with improved performance in terms of detailing requirements, damage tolerance, and repair needs when subjected to large inelastic deformation reversals.

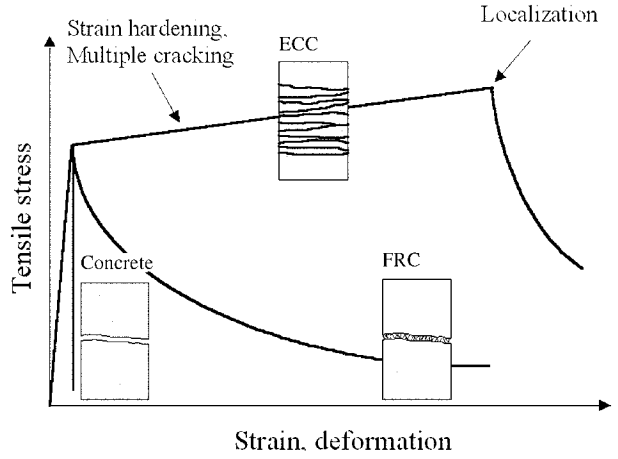

Fig. 1—Schematic stress-strain behavior of cementitious matrices in tension.

CEMENTITIOUS COMPOSITES CHARACTERISTICS

The comparison between R/ECC and RC is based on the material properties of both cementitious matrices. Engineered cementitious composites and concrete have similar ranges of tensile and compressive strengths (4 to 6 MPa and 30 to 80 MPa, respectively); however, their tensile deformation behavior is distinctly different. Whereas concrete in tension fails in a brittle manner upon reaching its cracking strength, ECC undergoes a strain-hardening phase analogous to that of metals (Fig. 1). Beyond formation of first cracking in the cementitious matrix, ECC is designed to increase its composite tensile stress up to strain levels on the order of several percent. In contrast to localized deformation in concrete and conventional FRC (Fig. 1), ECC accommodates imposed tensile deformations by formation of uniformly distributed multiple cracking with small individual crack widths (< 200 μm). Tensile failure of ECC is observed when the tensile strength of a crack bridged by fibers is reached, resulting in localized deformation at this section (Fig. 2(a)).

Due to its tensile deformation behavior, ECC represents one type of high-performance fiber-reinforced cement composites (HPFRCC), which are classified according to strain hardening and multiple cracking criteria (Naaman and Reinhardt 1995). These distinct material properties are expected to significantly influence the response of R/ECC structural members described in this paper. The design basis and mechanical properties of ECC are reviewed elsewhere (Li 1998).

In compression, ECC has a lower elastic stiffness compared to concrete, as well as larger strain at reaching its compressive strength, due to the lack of large aggregates. Beyond ultimate, the compressive stress drops to approximately $0.5f_c'$ with subsequently descending stress at further increasing deformation (Fig.2(b)).

Previous research on the shear resistance of ECC suggested assuming the mechanical properties in shear similar to those in tension (Li and Mishra 1996). The shear capacity of ECC is expected to have a major influence on minimizing the required amount of transverse steel reinforcement to resist shear forces in flexural members.

R/ECC RESPONSE CONCEPT

The behavior of R/ECC structural composites is constituted by the material properties of longitudinal steel reinforcement

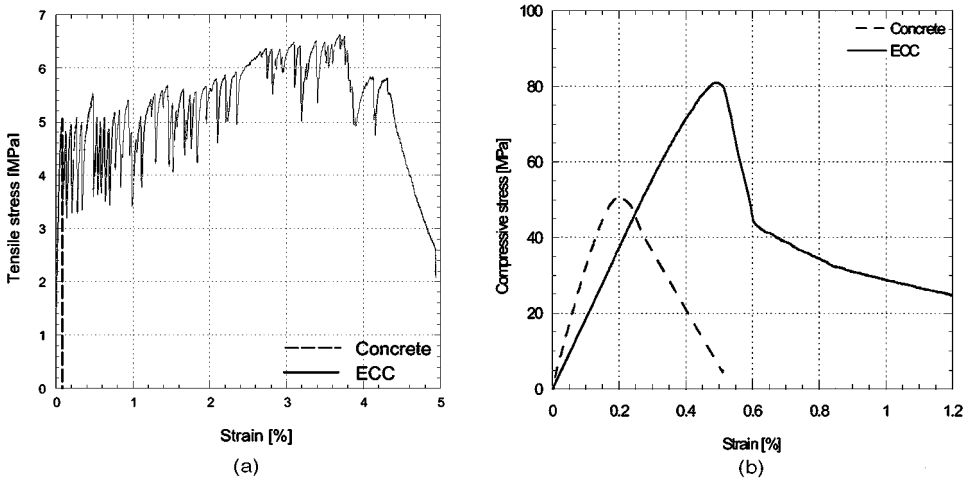

Fig. 2—(a) Stress-strain behavior of concrete and ECC in tension; and (b) stress-strain behavior of concrete and ECC in compression.

and ECC matrix as well as their interaction. Reinforced ECC structural composites can be considered a combination of ductile cementitious matrix (ECC) reinforced with a ductile element (steel) and, therefore, strain hardening and multiple cracking characteristics of ECC and the plastic yielding of steel reinforcement are essential determinants for their composite response mechanism.

Previous research on the interaction between ECC and steel reinforcement in uniaxial tension has shown that both materials deform compatibly in the inelastic deformation regime, resulting in a uniform strain distribution along the tensile specimen, elimination of interfacial bond stresses and bond-splitting failure, and improved tension-stiffening behavior in the elastic and inelastic range (Fischer and Li 2002). It is expected that these characteristics will also benefit the flexural response of R/ECC members, especially under reversed cyclic loading conditions with large inelastic deformations.

The anticipated inelastic response of R/ECC members under flexural load reversals is determined by the composite behavior in tension and compression, member shear resistance, matrix confinement effect, and resistance against buckling of longitudinal steel reinforcement. Considering the material properties of ECC and previous findings on the deformation mechanisms of R/ECC in tension, the inelastic flexural response can be described by two conceptual stages before and after transition from multiple cracking to localization of cracking. The description of these stages will focus on the inelastic response of R/ECC; however, prior to yielding of steel reinforcement, the ductile deformation behavior of ECC will also affect the flexural member response by a more uniform distribution of flexural cracking with reduced crack spacing and individual crack widths compared to reinforced concrete composites.

Beyond yielding of steel reinforcement and prior to localization of cracking in the ECC matrix, a given displacement of the R/ECC flexural member is expected to require a reduced peak curvature in the plastic hinge region compared with the RC composite, resulting in reduced sectional demand on reinforcement tensile strain and compressive stress in ECC. This reduction of peak curvature is related to an extended distribution of deformation along the flexural member, in particular beyond yielding of the longitudinal reinforcement (Fig. 3). Similar to the structural composite deformation mechanism in uniaxial tension, the distribution of deformation is due to the simultaneous strain hardening of ECC and steel reinforcement. Besides reduced sectional demand, interfacial bond stresses are negligible due to compatible deformation between reinforcement and ECC and radial bond-splitting forces are not generated. Consequently, longitudinal bond-splitting cracks will not occur, which is expected to prevent interfacial bond deterioration, cover spalling and composite disintegration under tension, and compression alternations. Thus, prior to localization of matrix cracking, the R/ECC member essentially benefits from a reduced sectional demand due to distributed flexural deformation along the specimen as opposed to localized crack formation observed in conventional RC members (Fig. 3).

In the second stage, the strain capacity of ECC at the cantilever base is exhausted at relatively large drift levels and localization of cracking leads to a concentration of deformation at this section. At this stage, the sectional demand is similar to that in RC and, consequently, deformation compatibility is lost and interfacial bond stresses are initiated. Slip between steel reinforcement and ECC causes radial stresses in the cementitious matrix, which in RC members

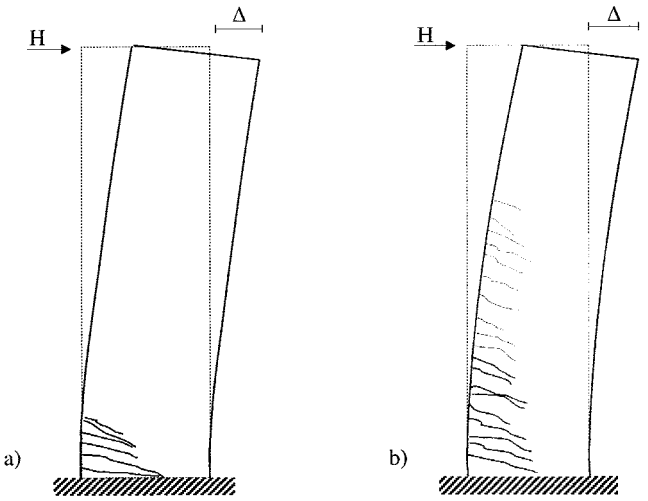

Fig. 3—Idealized flexural deformation behavior of: (a) RC and (b) R/ECC beyond yielding.

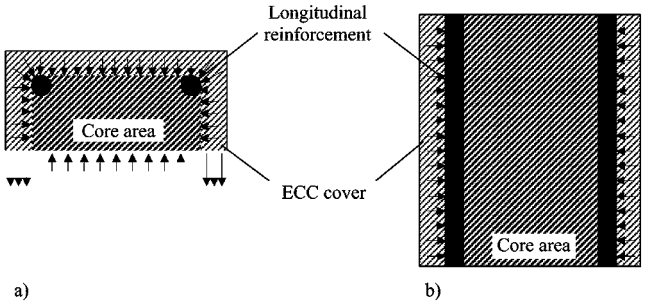

Fig. 4—Confining effect of ECC matrix in: (a) cross section; and (b) elevation.

leads to bond-splitting and spalling of the concrete cover (Goto 1971). In R/ECC, bond-splitting cracks may occur beyond localization of flexural cracking in ECC; however, in the transverse direction, ECC remains in the strain hardening regime with continuing resistance against cover spalling and reinforcement buckling. At this deformation stage, the R/ECC member benefits from the tensile strength of ECC beyond cracking, more specifically its confining effect and resistance against cover spalling.

Throughout both deformation stages, ECC is expected to resist other undesirable failure modes. Due to the intrinsic shear strength of ECC, additional transverse reinforcement provided by stirrups in potential plastic hinge regions and outside may be significantly reduced. Moreover, the confinement effect of the ECC cover provides lateral resistance against buckling of steel reinforcement in the form of a continuous embedment similar to the effect of a confining jacket, which is additionally anchored into the ECC core by means of fiber bridging (Fig. 4). The same mechanism is also expected to actively confine the ECC core, resulting in a ductile failure mode in compression. In this self-confining mechanism, the lateral expansion of ECC under axial compression is resisted by circumferential confinement exerted by the fibers in tension.

With respect to structural ductility, the most important contribution of ECC to the structural response of the member is to maintain composite integrity and provide lateral stability for the reinforcing steel to endure cyclic inelastic deformations without buckling. Despite its ductility in uniaxial tension, the cyclic behavior of ECC differs from that of a ductile metal,

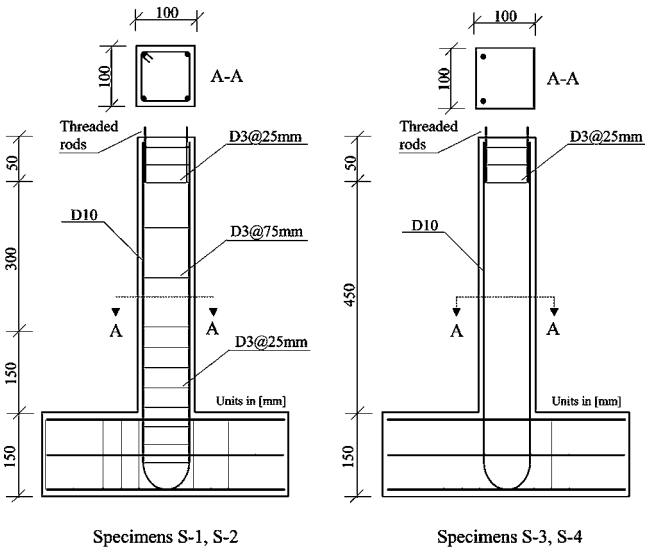

Fig. 5—Specimen configurations.

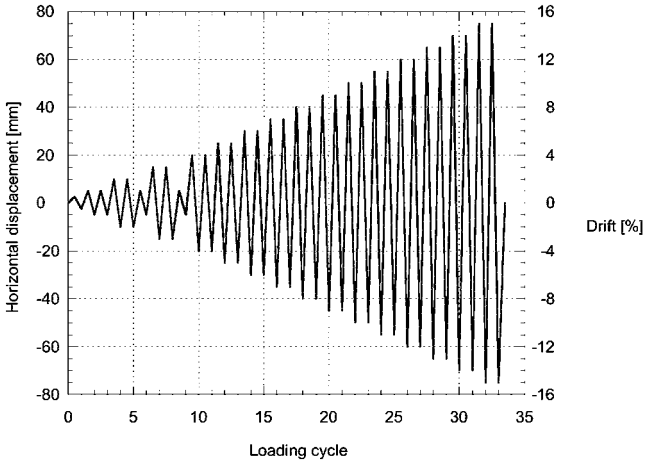

Fig. 6—Loading sequence.

in that ECC is unable to recover its energy dissipation capability under alternating inelastic tensile and compressive deformations. Therefore, direct contributions of ECC to member flexural strength and energy dissipation are expected to be relatively small. Its stabilizing effect on the longitudinal steel reinforcement and damage tolerance at large deformations, however, is expected to considerably improve structural performance with respect to member energy dissipation and damage evolution.

MATERIAL COMPOSITION AND PROPERTIES

The ECC matrix used in this particular study utilized 1.5% volume polyethylene fibers, cement, fine aggregates (maximum grain size 0.25 mm), water, a high-range water-reducing admixture, and admixtures to enhance the fresh properties of the mixture. Material properties in uniaxial tension obtained from this composition were a first cracking strength of 4.5 MPa at 0.01% strain and an ultimate tensile strength of 6.0 MPa at approximately 3.8% strain (Fig. 2(a)). The compressive strength of this ECC was 80 MPa at a strain of 0.50% (Fig. 2(b)).

Concrete used coarse aggregates (maximum grain size 10 mm), cement, water, and a high-range water-reducing admixture to enhance the fresh properties of the mixture. Tensile tests on concrete were not conducted but were assumed to have a first cracking strength similar to that of ECC (4.5 MPa at 0.01% strain) and subsequent brittle failure. The compressive strength of concrete used in this study was 50 MPa at a strain of 0.20% (Fig. 2(b)).

The longitudinal steel reinforcement in all specimen configurations had a ribbed surface geometry, a yield strength of 410 MPa at 0.2% strain, and an ultimate strength of 620 MPa at 14% strain. Transverse steel reinforcement had a smooth surface and a yield strength of 315 MPa at 0.2% strain. Due to the small size of the specimens used in this investigation, small-diameter longitudinal reinforcement was necessary to reflect realistic reinforcement ratios. The availability of conventional steel reinforcement, however, was limited to a minimum diameter of 10 mm. Transverse reinforcement with a smaller diameter was provided by steel wire with a smooth surface.

EXPERIMENTAL PROGRAM

Specimen and loading configuration

The structural behavior of R/ECC flexural members was experimentally investigated and compared to RC using small-scale cantilever beams (1/5 scale) with 500 mm height and square cross-sectional dimensions of 100 mm (Fig. 5). To provide cantilever-type loading conditions, a rigid transverse beam was integrally cast with the cantilever base. This loading configuration was chosen to promote a flexural deformation mode in all specimens and to investigate the effect of ECC material properties on the expected plastic hinge region in particular. Longitudinal steel reinforcement was bent at a 90 degree angle at the bottom of the transverse beam and further extended to provide sufficient anchorage (Fig. 5). Lateral loading was applied through a loading frame equipped with a 100 kN-capacity actuator according to a displacement-controlled loading sequence (Fig. 6). A steel pin was mounted on top of the cantilever to introduce the lateral load while the transverse beam was fixed to the base of the loading frame (Fig. 7). To investigate the influence of axial loading, external steel tendons were attached between the pin and the loading frame and tensioned by hydraulic actuators (Fig. 7).

The specimens were instrumented with a displacement transducer at the top of the cantilever to measure and control the deflection of the specimen. In addition, black-colored dots at 20 mm vertical spacing were spray painted on the surface of the specimen to assess sectional deformations and the specimen curvature distribution by means of an image analysis technique.

In this paper, a selection of specimens is presented that is part of a research project involving several types of reinforcing materials, including steel and various types of fiber-reinforced plastics (FRP). For the purpose of investigating the effect of matrix ductility on the structural response of steel reinforced members, the longitudinal steel reinforcement ratio was identical in all R/ECC and RC control specimens presented herein. Longitudinal reinforcement was provided by four reinforcing bars (∅ 10 mm), arranged symmetrically relative to both axes (Fig. 5), resulting in a total longitudinal reinforcement ratio of $\rho_{longitudinal} = 3.14\%$. This ratio is relatively high due to minimum available reinforcement diameters, however, within the required limits for flexural and axially loaded members (ACI Committee 318 1999). A clear cover of 10 mm was provided in all specimens.

Results from tests of four different specimen configurations are presented, specifically an RC control specimen with transverse reinforcement (S-1), an R/ECC specimen with

Table 1—Summary of specimen configurations

Specimen	Composite	Axial load	Reinforcement ratio		Yielding		Ultimate	
			$\rho_{longitudinal}$ *	$\rho_{transverse}$ †	Predicted‡	Observed§	Predicted‖	Observed§
S-1	RC	—	3.14	0.57/0.19	9.6	10.7	10.2	13.8
S-2	R/ECC	—	3.14	0.57/0.19	9.8	12.0	10.7	16.0
S-3	R/ECC	—	3.14	—	9.8	12.0	10.7	16.5
S-4	R/ECC	80 kN	3.14	—	15.1	17.0	16.4	19.0

*Total longitudinal reinforcement ratio (%).
†Transverse reinforcement ration below h = 150 mm/above h = 150 mm (%).
‡Predicted shear force (kN) at yielding.
§Observed shear force (kN).
‖Predicted shear force (kN) based on 0.003 and 0.006 limit strain in concrete and ECC, respectively.

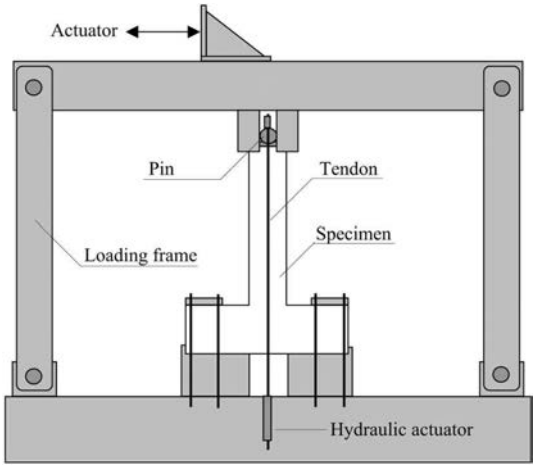

Fig. 7—Loading configuration.

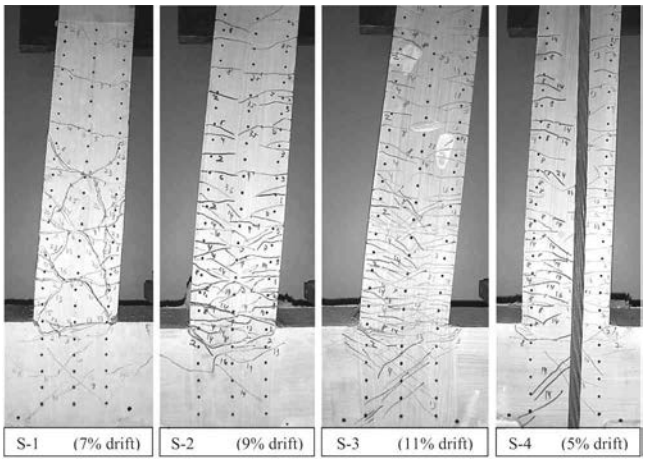

Fig. 8—Deflected shape and damage pattern of specimens at ultimate load.

transverse reinforcement (S-2), an R/ECC specimen without transverse reinforcement (S-3), and an R/ECC specimen without transverse reinforcement and an applied axial load of 80 kN (S-4), corresponding to 10% of the axial load-carrying capacity. Details of the specimen configurations are summarized in Table 1.

In two specimen configurations (S-1, S-2), transverse reinforcement was provided by stirrups (∅ 3 mm) with 135 degree hooks spaced at 25 mm ($\rho_{transverse}$ = 0.57%) in the joint region and at the base of the cantilever (h = 150 mm) and at 75 mm spacing above ($\rho_{transverse}$ = 0.19%). In all specimens, four threaded rods were placed at the top of the cantilever prior to casting and confined with stirrups (∅ 3 mm) at 25 mm spacing to mount the loading pin (Fig. 5). The pin was welded to a steel plate, which was then attached to the specimen with an adhesive and additionally tied to the threaded rods.

EXPERIMENTAL OBSERVATIONS

In Specimen S-1 (RC, with transverse reinforcement) prior to yielding, flexural cracks formed and propagated beyond the specimen centerline between the cantilever base and 300 mm height at an approximate crack spacing of 60 mm. At this stage, a maximum crack width of 0.2 mm was measured at the cantilever base; shear cracking along the specimen and in the joint region was not observed. Specimen S-1 entered the inelastic deformation regime as predicted at 1.5% drift corresponding to a nominal yield curvature of 0.000034 1/mm (Fig. 9(a)). Theoretical predications were based on the material properties of steel and concrete with a maximum allowable strain of 0.003 in compression. The measured shear force at yielding (10.7 kN) exceeded the predicted value (9.6 kN) based on yield strength of the reinforcing steel. Beyond yielding, the number of flexural cracks remained constant; however, the maximum observed flexural crack width increased to 0.5 mm. At 2% drift, shear crack formation at the cantilever base as well as in the joint region was initiated. The existing flexural cracks increased in width especially at the cantilever base to accommodate the induced displacements at the top of the cantilever. At 5% drift, shear and flexural cracks had formed several connected crack paths through the thickness of the specimen, and opening of these crack paths in shear contributed to the total deformation of Specimen S-1 at this stage. These deformation characteristics led to a loss of stiffness at the transition between alternating loading stages also known as pinching. Ultimate strength was obtained at 7% drift (Fig. 8) at a lateral load of 13.8 kN, which exceeds the nominal strength with a predicted shear force of 10.2 kN based on 0.003 limit strain in concrete, modeled in the analysis by Hognestad's parabola with linear tail (Hognestad, Hansen, and McHenry 1955). Bond splitting and spalling of concrete cover became apparent beyond 7% drift and coincided with a decrease in applied shear force at subsequent displacement stages. Failure of Specimen S-1 was caused by combined shear and compression failure of the concrete core at 9% drift. Based on a residual strength of 80% of ultimate strength, Specimen S-1 reached a maximum ductility of μ = 6.

Specimen S-2 (R/ECC, with transverse reinforcement) showed an average flexural crack spacing of 30 mm prior to yielding with crack propagation of approximately 40 mm from the respective tension side. Crack widths at this loading stage ranged from 0.05 mm at the cantilever base to 0.01 mm at the top. Yielding occurred at 2% drift at a shear force of 12.0 kN (Fig. 9(b)), which exceeds predicted values at yield

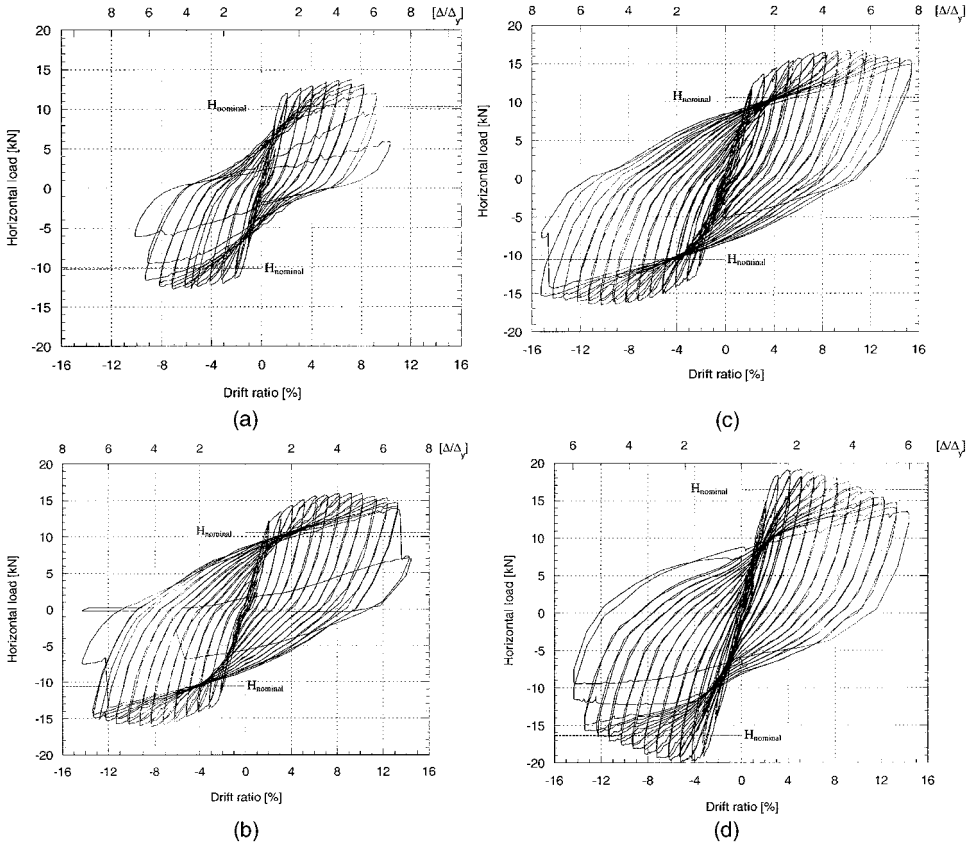

Fig. 9—Load-deformation behavior of: (a) Specimen S-1 (RC, with transverse reinforcement; (b) Specimen S-2 (R/ECC, with transverse reinforcement; (c) Specimen S-3 (R/ECC, without transverse reinforcement; and (d) Specimen S-4 (R/ECC, without transverse reinforcement).

of 9.8 kN at a curvature of 0.000037 1/mm, corresponding to 1.65% drift. Theoretical predications were based on the material properties of steel and ECC with a maximum allowable strain of 0.006 in compression. Beyond yielding, the average flexural crack spacing decreased to 20 mm accompanied by a maximum crack width of 0.2 mm and further propagation towards the specimen centerline. Flexural cracking extended approximately 40 mm into the joint region. At 5% drift, localization of cracking in the ECC matrix was observed. Prior to localization, the average crack spacing was 15 mm extending from the cantilever base to h = 400 mm with a maximum crack width of 0.4 mm, which exceeds the steady-state crack width of ECC; however, the interaction with structural steel reinforcement delayed localization in the flexural member. At this deformation stage, the average inclination of cracks suggested a flexure-dominated deformation mode with a limited number of fine shear cracks in the plastic hinge region. The ultimate strength of Specimen S-2 was reached at 9% drift (Fig. 8) at an applied shear force of 16.0 kN that compares with a predicted maximum shear force of 10.7 kN. At this deformation stage, flexural crack opening was concentrated at the cantilever base, while other flexural cracks stabilized in number and maximum crack width. Failure was caused by rupture of the steel reinforcement at 14% drift preceded by minor crushing of the ECC cover on the compression side. Throughout the test, bond splitting, spalling, and buckling of longitudinal reinforcement were not observed. Specimen S-2 provided a maximum ductility of μ = 6.5 at 80% residual strength.

Prior to yielding, specimen S-3 (R/ECC, without transverse reinforcement) showed a more extensive distribution of flexural cracking along the specimen compared to S-2 with an average crack spacing of 20 mm. Flexural cracking extended below the cantilever base at this stage of loading due to the lack of transverse reinforcement in the joint region. Yielding occurred at 2% drift at an applied lateral load of 12.0 kN (Fig. 9(c)) compared with a predicted shear force at yielding of 9.8 kN at 1.65% drift. At 5% drift, the number of flexural cracks increased in particular in the plastic hinge region where the average crack spacing was approximately 5 mm. Except in the joint region, only a few minor shear cracks were observed at this deformation stage, especially near the top of the specimen. Localization of cracking in the ECC matrix was observed at 7% drift. The flexural strength was reached at 10% drift at an applied load of 16.5 kN (Fig. 8) that compares with nominal strength at a lateral load of 10.2 kN. Specimen S-3 failed at 15% drift due to rupture of the longitudinal reinforcement coinciding with a maximum ductility of μ =7.5.

Specimen S-4 (R/ECC, without transverse reinforcement, axial load) had an externally applied axial load ($0.10A_c f_c'$) that was monitored and maintained constant during the test. Yielding occurred at a lateral applied load of 17.0 kN at a 2.4% drift (Fig. 9(d)) that compares with predicted values at yielding of 15.1 kN at 2% drift. Prior to yielding, well-distributed flexural cracks formed between the cantilever base and 350 mm height with an average spacing of 15 mm and length of 25 mm. At this stage, shear cracking in the joint

Table 2—Maximum curvature and plastic hinge length

Specimen	Nominal ϕ_y*	Ultimate ϕ_u†	2% drift		5% drift		7% drift		10% drift	
			ϕ_{peak}‡	L_p/h§	ϕ_{peak}‡	L_p/h§	ϕ_{peak}‡	L_p/h§	ϕ_{peak}‡	L_p/h§
S-1	0.000034	0.000188	0.000200	1.5	0.000500	1.6	0.000800	1.6	—	—
S-2	0.000037	0.000426	0.000220	1.2	0.000380	1.9	0.000570	2.2	0.001100	1.7
S-3	0.000037	0.000426	0.000220	1.5	0.000550	1.9	0.000750	2.6	0.001070	2.4

*Based on yield strength of longitudinal reinforcement [1/mm].
†Based on 0.003 and 0.006 limit strain in concrete and ECC, respectively [1/mm].
‡From image analysis.
§Length of plastic hinge L_p including yield penetration into joint.

region was not observed. Beyond yielding, the number and length of flexural cracks increased as well as the extent of shear crack formation in the joint region. At 5% drift, the ultimate strength of Specimen S-4 was reached at a shear force of 19.0 kN, accompanied by flexural crack localization, crushing of the ECC cover, and formation of shear cracking at the cantilever base (Fig. 8). Despite the lack of transverse steel reinforcement in the joint and the cantilever, shear failure did not occur. Similarly, crushing of the ECC cover did not result in cover spalling and the integrity of the plastic hinge section was maintained. At 10% drift, the tendency of the longitudinal reinforcement to buckle resulted in formation of longitudinal splitting cracks in the ECC cover; however, ECC remained in the strain hardening deformation regime. At 80% residual strength, S-4 showed a maximum ductility of $\mu = 5$. Further increasing flexural displacement increased damage by ECC crushing and lateral expansion of the plastic hinge region. Ultimately, failure of Specimen S-4 occurred at 14% drift by buckling of longitudinal reinforcement.

Image analysis

To monitor the deformation of Specimens S-1, S-2, and S-3, images of the specimens were taken with a digital camera (1150 x 960 resolution) at reaching the respective target displacement at each drift level. These digital images were then analyzed using image analysis software to obtain the coordinates of dots painted on the specimen surface. The deflected shape was deduced from the centerline of the specimen and approximated by a polynomial. Subsequently, deflection angle and curvature distribution along the specimens were derived. In previously conducted experiments, the deflected shape obtained by this method was compared to measurements taken by displacement transducers located at 100 mm spacing along the specimen and reasonable agreement between both sets of displacement readings was found. The sensitivity of this method is proportional to the resolution of the images obtained that in this study resulted in displacement measurements with an accuracy of approximately 0.5 mm.

Similar attempts to determine specimen deformations by means of image analysis were presented in another study (Ma, Bertero, and Popov 1976) and involved analog inspection of the photographic images that caused some difficulty in accurately locating the predefined sample points on the specimen.

While the method used in this study at the given image resolution provides satisfactory data for total deflection measurements, the accuracy obtained is not sufficient to quantitatively extract the shear distortion along the tested specimens, especially considering the ratio of specimen height to width and the resulting magnitude difference between total deflection and shear distortions. Therefore, deflection measurements as well as the derived deflection angle and curvature considered herein contain contributions from flexural and shear deformation components.

To compare the deformation distribution at increasing displacements, images taken of the specimens at 2% drift, 5% drift, 7% drift, and at ultimate have been selected and processed as described previously. The curvature distributions of Specimens S-1, S-2, and S-3 (Fig.10 (a) to (c)) indicate the deformation characteristics at positions between the joint region 100 mm below the cantilever base and 300 mm cantilever height. In addition, the respective nominal yield curvature of each specimen configuration is shown. Experimental results obtained from image analysis are summarized in Table 2.

In specimen S-1 (RC, with transverse reinforcement), the maximum curvature at each considered drift level is located at the cantilever base with increasing displacements resulting in increased maximum curvature (Fig. 10(a)). Beyond yielding at 1.5% drift, the maximum curvature at 2% drift is 0.00020 1/mm. At 5% drift and at ultimate (7% drift), the maximum curvature along Specimen S-1 increases to 0.00048 1/mm and 0.00080 1/mm, respectively. Inelastic deformation propagates approximately 60 mm below the column base into the joint region and extends 100 mm into the cantilever. The extent of plastic deformation is constant; however, its magnitude increases at increasing displacement levels. At positions above 100 mm height, negative curvatures are caused by inelastic deformations due to shear cracking, in particular at ultimate (7% drift). The peak curvature readings obtained from image analysis of Specimen S-1 agree well with those reported in another study, in which tests on RC specimens of similar geometry and loading configuration had been conducted (Aycardi, Mander, and Reinhorn 1994).

In Specimen S-2 (R/ECC, with transverse reinforcement), the peak curvature at 2% drift is similar to that in Specimen S-1, however, located above the cantilever base at $h = 40$ mm and plastic curvature extending approximately 20 mm into the joint region (Fig. 10(b)). At increasing drift levels, the maximum curvature is 0.00040 1/mm and 0.00057 1/mm at 5% drift and 7% drift, respectively. The plastic hinge length increases with increasing drift extending in both directions into the cantilever as well as into the joint region. At 7% drift, the total plastic hinge length of Specimen S-2 is 240 mm as compared with 190 mm in Specimen S-1. At 10% drift, the peak curvature is 0.00115 1/mm. Similar to Specimen S-1, negative curvature readings above the plastic hinge are influenced by inelastic shear deformations and damage in the specimen.

DISCUSSION

The verification of the effect of substituting concrete with ECC in a flexural member is based on direct comparison between Specimen S-1 (RC, with transverse reinforcement) and Specimen S-2 (R/ECC, with transverse reinforcement), both with identical reinforcement detailing. The behavior of Specimens S-3 (R/ECC, without transverse reinforcement) and S-4 (R/ECC, without transverse reinforcement, axial load) is then contrasted to Specimen S-2 to draw further conclusions.

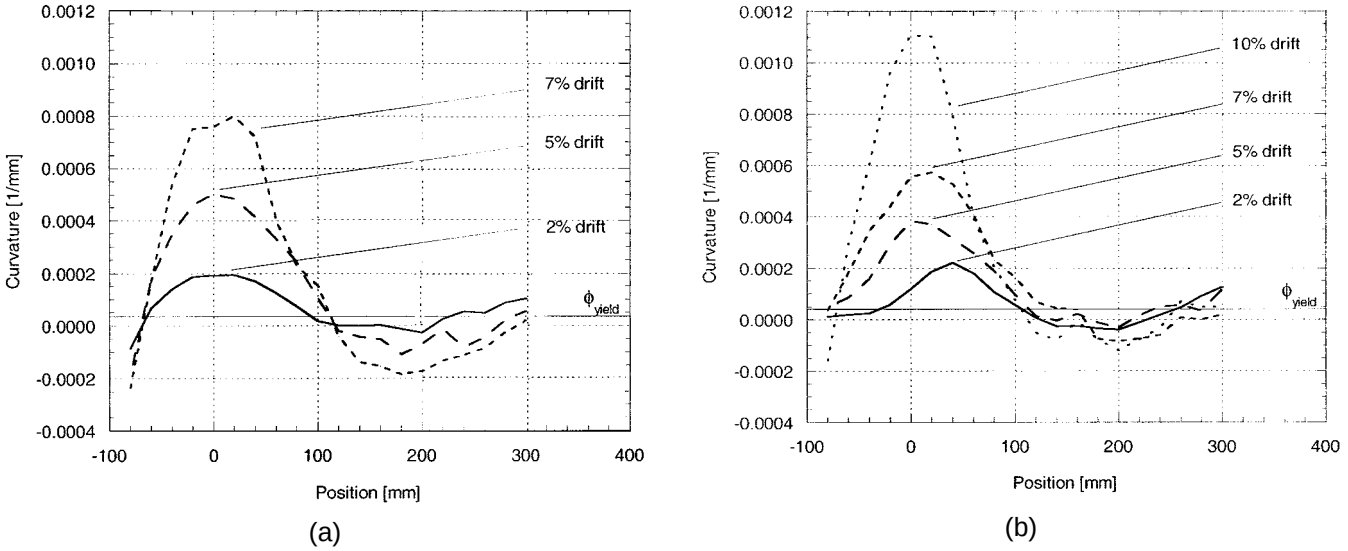

Fig. 10—(a) Curvature distribution on Specimen S-1; and (b) curvature distribution on Specimen S-2.

Load-deformation response

The lateral load-deflection curves (Fig. 9(a) to (d)) indicate a flexural failure mode of all specimens at applied loads exceeding the nominal capacity as predicted by flexural strength calculations, assuming a maximum strain capacity of 0.003 for concrete and 0.006 for ECC. In all cases, nominal strength was determined neglecting the tensile strength contribution of the cementitious matrix. The flexural overstrength observed can be attributed to strain hardening of the steel reinforcement and in RC (S-1) partially to the confinement effect of transverse reinforcement. The effect of reinforcement strain hardening is more significant in R/ECC specimens (S-2, S-3) that fully use the strain capacity and ultimate tensile strength of the steel reinforcement. In RC (S-1), premature failure in shear and compression limits the extent of strain hardening in the longitudinal reinforcement and consequently results in smaller overstrength compared to the R/ECC specimens.

The ultimate flexural strength of Specimen S-1 is reached at 7% drift (Fig. 9(a)), limited by composite deterioration due to shear cracking as well as crushing and spalling of the concrete cover in the plastic hinge region. At further increasing displacement, continuing composite disintegration leads to failure at 9% drift.

In Specimen S-2 (Fig. 9(b)), the direct contribution of tensile load-carrying capacity of ECC to the flexural resistance is lost at localization of tensile cracking in the ECC matrix at 5% drift, corresponding to the transition from the stage of reduced sectional demand to increased composite resistance, as outlined in the response concept. This transition, however, is smooth and does not significantly affect the load-deformation response. Beyond this point, the flexural resistance continues to increase and reaches its peak at 9% drift. At further increasing displacement, the ductile deformation characteristics of ECC prevent failure by cover crushing and spalling, shear cracking, or buckling of longitudinal reinforcement, and result in a ductile postpeak response of Specimen S-2. Due to the number of cycles at relatively large inelastic deformations, low-cycle fatigue failure of the steel reinforcement occurs at 14% drift and testing is terminated.

The comparison of load-deformation response of Specimen S-2 (R/ECC, with transverse steel reinforcement) and Specimen S-3 (R/ECC, without transverse reinforcement) indicates virtually identical behavior (Fig. 9(c)). The elimination of transverse steel reinforcement does not negatively affect the performance of Specimen S-3 in terms of load-deformation response, flexural strength, and damage evolution. The ultimate strength of Specimen S-3 is obtained at a slightly larger displacement (16.8 kN at 10% drift) as compared with Specimen S-2 (16 kN at 9% drift). The minute difference in flexural strength may be explained by yield propagation into the joint region due to lack of transverse reinforcement and resulting change in the internal stress distribution at this section.

In the case of axial loading, the flexural stiffness of Specimen S-4 (R/ECC without transverse reinforcement, axial load) is higher compared with Specimens S-2 and S-3 due to the effect of axial load on the sectional stress and strain distribution (Fig. 9(d)). In addition, the horizontal contribution of the externally applied axial, centrally guided load affects the measured lateral load applied through the actuator; however, its vertical component outweighs this contribution due to the resulting P-δ effect. Therefore, the load-deformation curve of Specimen S-4 (Fig. 9(d)) has not been modified to account for these counteracting effects of the externally applied load on the flexural response. Peak lateral load is obtained at 5% drift beyond which the flexural resistance decreases by ductile crushing of the ECC matrix. Similar to Specimens S-2 and S-3, the postpeak behavior of Specimen S-4 is ductile due to the deformation characteristics of ECC in compression and preserved composite integrity in the plastic hinge region. Ultimately, the confinement effect of the ECC cover is exhausted at 14% drift and failure occurs by buckling of longitudinal reinforcement.

Energy dissipation

To evaluate the effect of matrix ductility on the energy dissipation capacity of the tested specimens, two different indices were employed to characterize the shape of the hysteresis curve and assess the cumulative energy absorbed in the inelastic deformation process (Priestley et al. 1994).

The equivalent damping ratio characterizes the shape of the hysteresis loops by relating the energy dissipated in one complete deformation cycle to the maximum strain energy at a given displacement amplitude (Chopra 1995). The

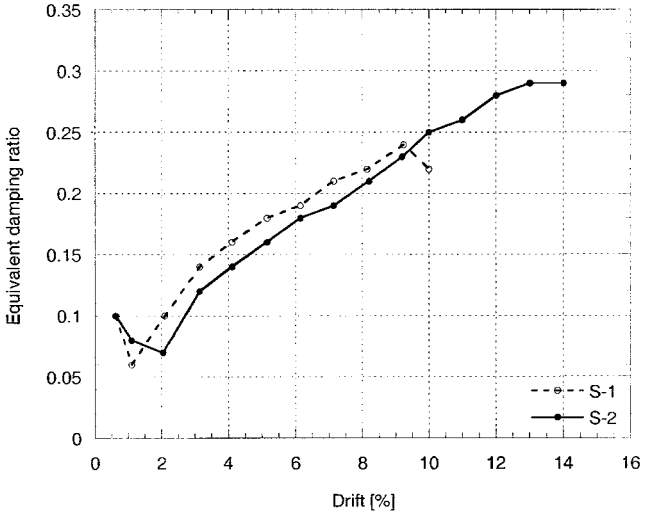

Fig. 11—Equivalent damping ratio of Specimens S-1 and S-2.

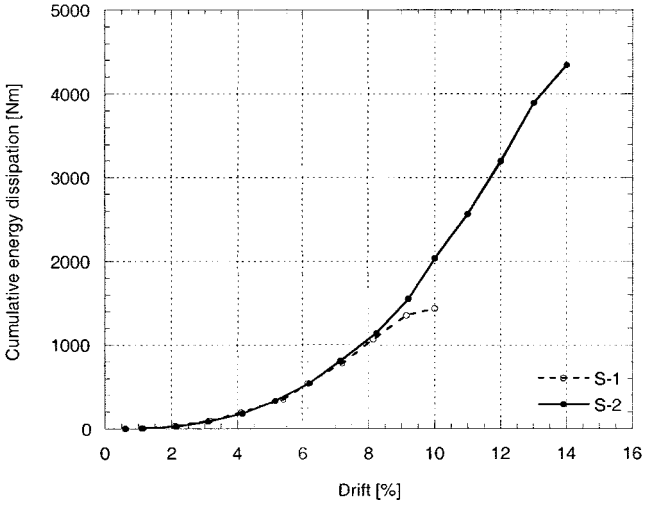

Fig. 12—Cumulative energy dissipation of Specimens S-1 and S-2.

comparison of Specimen S-1 and S-2 indicates slightly higher equivalent damping in RC (Fig. 11) due to lower flexural resistance, that is, lower strain energy at a given displacement relative to R/ECC.

The cumulative dissipated energy (Fig. 12) in both specimens is virtually identical at drift levels prior to S-1 reaching its ultimate strength at 7% drift. While the RC specimen has little energy dissipation capacity beyond ultimate due to rapid strength degradation, R/ECC shows steadily increasing cumulative energy dissipation until failure by rupture of steel reinforcement.

The comparison of RC and R/ECC in terms of equivalent damping and cumulative energy dissipation indicates that the ductile stress-strain deformation behavior of ECC in uniaxial tension has insignificant direct effect on the energy dissipated in cyclic loading, while the inelastic deformation of steel reinforcement comprises the predominant contribution. Therefore, preserving this inelastic deformation mechanism by reinforcement yielding is of crucial importance to the performance of the structural member with respect to energy dissipation capacity. In RC members, the inelastic strain capacity of steel reinforcement cannot be fully utilized due to premature failure by shear and compression in Specimen S-1. Thus, in R/ECC (S-2, S-3), the most significant benefit of ECC ductility with respect to inelastic deformation behavior and energy dissipation is to maintain lateral stability of the longitudinal reinforcement to assure cyclic inelastic deformations at large displacement levels.

Transverse reinforcement requirements

In Specimen S-1 (RC), transverse reinforcement is essential for satisfactory performance, especially under reversed cyclic loading conditions. In R/ECC, the comparison of Specimens S-2 and S-3 (Fig. 9(b), (c)), however, shows nearly identical behavior with and without transverse reinforcement, which indicates the effectiveness of substituting transverse steel reinforcement with ECC for shear resistance and prevention of reinforcement buckling. Similar to Specimen S-2, failure of Specimen S-3 occurs by rupture of the longitudinal steel reinforcement. Therefore, lower-bound shear strength of ECC can be approximated by the peak shear force measured in Specimen S-3 normalized by the gross cross-sectional area of the specimen, resulting in shear strength of 1.5 MPa, which is comparable to the shear strength provided by steel reinforcement in the RC specimen (S-1). This approximation neglects the contribution of dowel action to member shear strength as well as the actual fraction of cross-sectional area engaged in resisting the applied shear force. Based on the observed peak shear force in Specimen S-4 (R/ECC, without transverse reinforcement, axial load), the lower-bound shear strength of R/ECC increases slightly; however, the effect of axial load is expected to have a significant influence on the composite shear resistance and may lead to less conservative estimates.

Considering the load-deformation behavior of Specimens S-2, S-3, and S-4, the experimental results obtained in this study on small-scale specimens suggest that transverse reinforcement may be significantly reduced or neglected in R/ECC flexural members at low axial load levels. Due to the self-confining effect of ECC and the predominant formation of flexural cracking at a given aspect ratio of the tested specimens, transverse reinforcement provided by stirrups for confinement and shear resistance is found redundant for the specimens presented herein.

Curvature distribution

Measurements of the curvature distribution in Specimens S-1 and S-2 confirm smaller peak curvature in R/ECC (Fig. 10(b)) compared with RC (Fig. 10(a)) at a given displacement beyond yielding, indicating reduced sectional demand in the plastic hinge region of the R/ECC member and confirming the assumptions made in the response concept. Strain-hardening deformation behavior of ECC and steel reinforcement and the resulting formation of distributed multiple cracking along the height of Specimen S-2 (Fig. 8) are responsible for this reduction of sectional demand that is compensated by an increased plastic hinge length to attain the target displacement. The fact that the extent of inelastic curvature in RC (S-1) remains nearly constant may be caused by interfacial debonding between reinforcement and concrete at initial yielding without further yield propagation and immediate engagement of reinforcement in the inelastic deformation process along the entire plastic hinge length. In contrast, the increasing plastic hinge length in Specimen S-2 is a result of successive activation of the ECC matrix in the inelastic de-

formation process due to strain hardening as tensile stresses on the matrix increase at increasing displacement levels.

Effect of axial load

The externally applied load in Specimen S-4 (R/ECC, without transverse reinforcement, axial load) leads to more extensive flexural cracking prior to yielding, larger specimen deflection at yielding, and increased ultimate strength (Fig. 9(d)) compared to Specimen S-2. Furthermore, strength decay of Specimen S-4 at relatively small drift is caused by compression failure of ECC due to the presence of axial load. Specimen S-4, however, maintains axial load-carrying capacity beyond ultimate as well as stable hysteretic behavior up to failure by buckling of the longitudinal reinforcement at 14% drift. Although it is possible to prevent this failure mode by providing transverse steel reinforcement, the drift level at failure of Specimen S-4 is excessive and unlikely to be achieved under realistic conditions.

Composite damage

The deformation behavior and failure mode of the tested specimens clearly indicate differences in the damage mechanisms, particularly between RC and R/ECC. While these differences are apparent from the condition of the specimens at increasing displacement levels, the quantification of damage based on experimentally obtained data is complicated. Furthermore, a distinction must be made between intended inelastic deformations by reinforcement yielding and detrimental damage by composite disintegration, which limits the stability and energy dissipation capacity of the member.

From the experimental data obtained in this study, only qualitative conclusions on the damage level can be drawn. The extent of shear cracking in RC and R/ECC is one indication for the different damage mechanisms in both composites. In R/ECC specimens (Fig. 9(b) to (d)), predominant flexural cracking especially in the plastic hinge region is responsible for the lack of pinching, which is apparent in R/C (Fig. 9(a)). In R/ECC, the shape of the hysteresis loops is alike at increasing inelastic drift levels, suggesting a persistent, flexural deformation mechanism. In contrast, the hysteresis loops in RC indicate the influence of shear cracking beyond 5% drift by a noticeable change in stiffness at the transition between alternating loads.

Furthermore, the failure mode in the RC and R/ECC specimens is distinctly different and implies that the member performance in RC is affected by the brittleness and damage of concrete in the plastic hinge region as opposed to low-cycle fatigue failure of steel reinforcement in R/ECC Specimens S-2 and S-3.

CONCLUSIONS

The comparisons of RC and R/ECC specimens presented herein indicate performance improvements resulting from the ductile deformation behavior of ECC. In particular, the energy dissipation capacity of R/ECC is significantly enhanced. This fact, however, is not adequately reflected in the ductility factor obtained from both composites and is better represented by the cumulative energy dissipation.

For the specimens presented in this study, the intrinsic shear capacity of ECC provides sufficient shear resistance for the R/ECC members. Additional transverse steel reinforcement is found ineffective in R/ECC flexural members at given aspect ratio and low axial load levels. Furthermore, ECC serves as lateral confinement for the longitudinal reinforcing bars and prevents premature failure by reinforcement buckling.

Damage in R/ECC members is dominated by flexural cracking of ECC and stable inelastic deformations of steel reinforcement. ECC shows considerably higher damage tolerance than confined concrete. Bond splitting and spalling of ECC as well as composite disintegration due to cyclic loading are prevented.

During the initial stage of member response prior to localization of flexural cracking in ECC, an extensive distribution of flexural deformation along the member leads to a reduction of sectional demand, especially in the plastic hinge region. The transition from multiple cracking to localized deformation—that is, from reduced sectional demand to increased composite resistance—however, is indistinguishable in the load-deformation response. More importantly, the ductility of ECC increases the resistance against composite deterioration beyond crack localization.

Despite the considerable tensile strength and strain capacity of ECC, its direct contribution to flexural strength and energy dissipation is negligible. The synergistic interaction between steel reinforcement and the ECC matrix, however, leads to improved performance of the flexural member as compared with conventional RC.

ACKNOWLEDGMENTS

The research described in this paper has been supported by a grant from the National Science Foundation (CMS-0070035) to the ACE-MRL at the University of Michigan. This support is gratefully acknowledged.

REFERENCES

ACI Committee 318, 1999, "Building Code Requirements for Structural Concrete (ACI 318-99) and Commentary (318R-99)," American Concrete Institute, Farmington Hills, Mich., 391 pp.

Aycardi, L. E.; Mander. J. B.; and Reinhorn, A. M., 1994, "Seismic Resistance of Reinforced Concrete Frame Structures Designed Only for Gravity Loads: Experimental Performance of Subassemblages," *ACI Structural Journal*, V. 91, No. 5, Sept.-Oct., pp. 552-563.

Chopra, A. K., 1995, *Dynamics of Structures—Theory and Applications to Earthquake Engineering*, Prentice-Hall, Inc., pp. 94-100.

Fischer, G., and Li, V. C., 2002, "Influence of Matrix Ductility on the Tension-Stiffening Behavior of Steel Reinforced Engineered Cementitious Composites (ECC)," *ACI Structural Journal*, V. 99, No. 1, Jan.-Feb, pp. 104-111.

Goto, Y., 1971, "Cracks Formed in Concrete Around Deformed Tension Bars," ACI JOURNAL, *Proceedings* V. 68, Apr., pp. 244-251.

Hognestad, E.; Hansen, N. M.; and McHenry, D., 1955, "Concrete Stress Distribution in Ultimate Strength Design," ACI JOURNAL, *Proceedings* V. 52, pp. 455-479.

Li, V. C., "Engineered Cementitious Composites—Tailored Composites Through Micromechanical Modeling," *Fiber Reinforced Concrete: Present and the Future*, N. Banthia, A. Bentur, and A. Mufti, eds., Canadian Society for Civil Engineering, Montreal, pp. 64-97.

Li, V. C., and Mishra, D., "Structural Applications of Engineered Cementitious Composites," *The Indian Concrete Journal*, V. 70, No. 10, pp. 561-574.

Ma, S. M.; Bertero, V. V.; and Popov, E. P., 1976, "Experimental and Analytical Studies on Hysteretic Behavior of Reinforced Concrete Rectangular and T-Beams," *Report* No. 76-2, Earthquake Engineering Research Center, University of California, Berkeley, Calif.

Naaman, A. E., and Reinhardt, H. W., 1995, "Characterization of High Performance Fiber Reinforced Cement Composites-HPFRCC," *Proceedings of High Performance Fiber Reinforced Cement Composites 2* (HPFRCC 2), A. E. Naaman and H. W. Reinhardt, eds.

Paulay, T., and Priestley, M. J. N., 1992, *Seismic Design of Reinforced Concrete and Masonry Buildings*, John Wiley & Sons, Inc., pp. 98-106.

Priestley, M. J. N.; Seible, F.; Xiao, Y.; and Verma, R., 1994, "Steel Jacket Retrofitting of Reinforced Concrete Bridge Columns for Enhanced Shear Strength-Part 2: Test Results and Comparison with Theory," *ACI Structural Journal*, V. 91, No. 5, Sept.-Oct., pp. 537-551.

Sheikh, S. A., and Yeh, C. C., 1990, "Tied Concrete Columns under Axial Load and Flexure," *ASCE Journal of Structural Engineering*, V. 116, No. 10, pp. 2780-2800.

Watson, S.; Zahn, F. A.; and Park, R., 1994, "Confining Reinforcement for Concrete Columns," *ASCE Journal of Structural Engineering*, V. 120, No. 6, pp. 1798-1823.